Astron. Astrophys. 336, 339–351 (1998)

ASTRONOMY AND ASTROPHYSICS

A search for precursors of ultracompact HII regions in a sample of luminous IRAS sources

II. VLA observations⋆

S. Molinari[1,2,3,⋆⋆], **J. Brand**[1], **R. Cesaroni**[4], **F. Palla**[4], **and G.G.C. Palumbo**[2,5]

[1] Istituto di Radioastronomia-CNR, Via Gobetti 101, I-40129 Bologna, Italy
[2] Università degli Studi di Bologna, Dipartimento di Astronomia, Via Zamboni 33, I-40126 Bologna, Italy
[3] Istituto di Fisica dello Spazio Interplanetario-CNR, Via G. Galilei, CP 27, I-00044 Frascati, Italy
[4] Osservatorio Astrofisico di Arcetri, Largo E. Fermi 5, I-50125 Firenze, Italy
[5] Istituto Te.S.R.E.-CNR, Via Gobetti 101, I-40129 Bologna, Italy

Received 1 September 1997 / Accepted 16 March 1998

Abstract. We have used the Very Large Array (VLA) to search for radio continuum emission towards a sample of 67 IRAS sources selected from a previous study. All observed sources are associated with high density molecular gas, exhibit an infrared spectral energy distribution characteristic of very cold young stellar objects and many of them are associated with H_2O masers. The observed sample is divided into two groups of sources: *High*, with IRAS spectral energy distributions resembling those of ultracompact HII regions, and *Low*, for which previously collected evidence suggests that they may contain a higher fraction of protostellar objects than the *High* group; such objects might not have started hydrogen burning yet.

Radio continuum emission was detected towards 37 sources (55%), although only in 22 cases an association with the IRAS source is established. Of the latter, 9 (24%) objects belong to the *Low* type and 13 (43%) to the *High* type. Thus, we find that 76% of *Low* and 57% of *High* sources are not associated with a radio counterpart. Because the majority of the sources have luminosities above $\sim 10^4\ L_\odot$, corresponding to central stars of spectral type between B2 and O7, the lack of radio emission is interpreted as being due to the action of accreting matter that chokes off the expansion of the ionised gas. We show that this requires only moderate mass accretion rates, below $\sim 10^{-4}\ M_\odot\ \mathrm{yr}^{-1}$. Alternatively, dust absorption can also effectively absorb UV photons and the gas column density implied by our observations indicates values in excess of $10^{22}\ \mathrm{cm}^{-2}$.

The physical properties of IRAS sources with associated radio counterpart derived from the present observations do not distinguish between *High* and *Low* sources. These sources are likely to be ZAMS stars with variable amounts of dust within the ionised region which acts as UV field absorber. The large majority of detected sources (75%) have spherical or unresolved morphology, while 15% are irregular or multiply peaked and only 10% have a core-halo structure. These results agree with the known properties of ultracompact HII regions, even though the average luminosity of the present sample is an order of magnitude lower than that in previous studies.

Key words: stars: formation – stars: pre-main sequence – stars: circumstellar matter – ISM: HII regions – sources as a function of wavelength: radio continuum: ISM

1. Introduction

This is the second of a series of papers aimed at studying the earliest phases of pre-stellar evolution of high mass Young Stellar Objects (YSOs). In our first work (Molinari et al. 1996, hereafter Paper I) we presented the results of the observations of (J,K)=(1,1) and (2,2) ammonia lines towards 163 IRAS sources which were part of a larger sample of 260 sources selected by Palla et al. (1991, hereafter P91). These sources, all characterised by a 60μm flux greater than 100 Jy, were selected from the IRAS Point Source Catalog, Version 2, according to the Richards et al. (1987) colour criteria for identifying compact molecular cores and for which no association with a known HII region was established in the literature (see P91 for details of other criteria). Following Wood & Churchwell (1989, hereafter WC89), P91 identified a subsample of 125 sources, which they called *High*, whose $[25-12] \geq 0.57$ and $[60-12] \geq 1.3$ colours are typical of IRAS sources associated with ultracompact (UC) HII regions; the remaining 135 sources were called *Low*.

P91 have searched the whole sample for H_2O maser emission and verified that the detection rate was three times larger in *High* sources than in *Low* sources, a finding which was regarded as a possible indication that the *Low* sources may be on average younger than *High*. Our ammonia observations (Paper I) were then used to restrict the sample to only those sources associated with dense molecular gas. Some differences in the gas properties

Send offprint requests to: molinari@ipac.caltech.edu

⋆ The tables, and the complete set of radio maps in the Appendix is available in electronic form at CDS via ftp 130.79.128.5

⋆⋆ Present address: IPAC/Caltech, Mail Stop 100-22, Pasadena CA 91125, USA

of *High* and *Low* sources were found; in particular the ratio of ammonia (2,2) and (1,1) linewidths was found to be correlated with the [25−12] colour.

Observations at radio wavelengths are then needed to identify the nature of the objects embedded in the circumstellar envelopes of *High* and *Low* sources. The radio continuum radiation observed towards HII regions is mainly due to bremsstrahlung of the plasma produced by the UV field of the central ZAMS star; hence we regard the lack of radio-continuum emission from bright infrared sources as a strong indication of extreme youth. In particular, most of the sources in the present work have luminosities typical of B0-ZAMS stars (Panagia 1973) whose Lyman continuum, coupled with the observational techniques used, should ensure their detection at radio wavelengths with the VLA. Only sources which were detected in ammonia lines (Paper I) were observed with the VLA. Due to limited observing time, we could not observe all NH_3-detected sources; the sample of prime interest is that of the *Low* sources because both P91 and Paper I suggest that they may be younger, so these were given the highest priority: we selected 37 *Low* sources (out of 38) and 30 *High* sources (out of 63). The latter were observed as a comparison sample and among them priority was given to sources with an associated H_2O maser (P91).

After a brief description of observational- and data reduction procedures in Sect. 2, the results are given in Sect. 3 and are discussed in Sect. 4. The main conclusions are summarised in Sect. 5.

2. Observations and data reduction

The Very Large Array of the National Radio Astronomy Observatory[1] was used on three occasions. In all runs all 27 antennas were always used with a bandwidth of 50 MHz; the signal was collected from both IFs. *Low* sources were observed at both 14939.9 and 4860.1 MHz (2 and 6 cm wavelength respectively) to determine their radio spectral slope; *High* sources were observed only at 4860.1 MHz.

2.1. Run I

On 26 June 1994, 35 *Low* sources were observed at 6 and 2 cm with the array in B configuration. The zenith synthesised beam widths expected for this configuration are $1\farcs2$ and $0\farcs4$ at the two wavelengths respectively. The actual angular resolution of the observations is less and in many cases the beam is far from circular: at 6 cm the beam width ranged from $1\farcs8 \times 1\farcs4$ to $4\farcs0 \times 1\farcs8$ (at 2 cm these figures must be divided approximately by three) depending on declination and hour angle of the source.

Integration times were 4 minutes at 6 cm and 9 minutes at 2 cm, resulting in a theoretical image r.m.s. of 0.15 mJy and 0.26 mJy respectively. The actual r.m.s. was lower due to the reduction technique used (see below). The primary calibrator was 3C286 and the assumed flux densities were 7.47 Jy and 3.40 Jy at 6 and 2 cm respectively; suitable phase calibrators were observed approximately every 20–25 minutes.

2.2. Run II

On 4 October 1994, 30 *High* sources and 5 *Low* sources (already observed during run I) were observed at 6 cm, and 2 *Low* sources (which were not visible in run I) at both 6 and 2 cm. The array was in the hybrid configuration CnB, resulting in beam widths ranging (at 6 cm) from $4\farcs0 \times 1\farcs7$ to $6\farcs5 \times 1\farcs7$. Five *Low* sources were observed again at 6 cm because they appeared extended or confused in the higher resolution observations of run I.

Integration times were approximately 4 minutes for each source. The primary calibrator was 3C48 with assumed flux densities of 5.48 Jy and 1.78 Jy at 6 and 2 cm respectively; phase calibrators were observed approximately every 20 minutes. For the two *Low* sources observed both at 6 and 2 cm, integration times were the same as used in run I.

2.3. Run III

On 23 and 24 January 1995, 9 *Low* sources, detected at 6 cm during run I and not detected at 2 cm during run I (possibly due to excessive spatial resolution), were re-observed at 2 cm . The array was in the hybrid configuration DnC and synthesised beam widths ranged from $3\farcs7 \times 1\farcs7$ to $9\farcs3 \times 1\farcs7$.

Integration times were approximately 20 minutes implying an image r.m.s. of 0.17 mJy; the primary calibrator was 3C286, with an assumed flux density of 3.40 Jy, and a suitable phase calibrator was chosen for each source.

2.4. Data reduction

The AIPS package was used for data reduction. Calibrator data were first edited and bad data flagged. The flux density of the primary calibrator was assigned and the procedure VLACALIB was used to calibrate the antenna gains for all secondary calibrators. This procedure was iterated until closure errors were $\leq$10%. Fluxes for secondary calibrators were derived and finally the procedure VLACLCAL was used to calibrate antenna phases.

The calibration table thus derived was applied and after data from various sources were SPLIT into single files, plots of uv visibilities were made to check data quality and bad data were flagged. Task MX was used to derive $5' \times 5'$ maps at 6 cm and $1\farcm7 \times 1\farcm7$ at 2 cm with natural weighting. The maps were then self-calibrated: first, we corrected the antenna phases by means of task CALIB using the brightest clean components as a source model, then a new map was built using MX. A few CALIB-MX iterations were needed to achieve an r.m.s. noise generally below the theoretical estimate. Task IMFIT was finally used to determine the properties of emission peaks (position, intensity and dimensions), and with IMEAN we derived the integrated flux density over a large region enclosing the source.

As data at different wavelengths were taken with different antenna configurations, the $u - v$ plane has been differently

[1] The National Radio Astronomy Observatory is operated by Associated Universities, Inc., under contract with the National Science Foundation.

sampled and this means that the data cannot directly be compared. To partially recover from this inconvenience the highest resolution observations were properly degraded; this was accomplished using task MX with a reconstruction beam equal to that of the lower resolution image.

3. Results

The results of the observations described above are listed in Tables 1a and b for *High* and *Low* sources respectively. In the tables we give: [Col. 1] source number as in Paper I followed by a code identifying, when applicable, multiple components within a source or multiple sources within a field (the number is printed in boldface and underlined if the radio source is considered associated with the IRAS source – see Sect. 3.3); [Col. 2] the wavelength in cm; [Col. 3] reference to the observing run in which the data were taken; [Cols. 4–5] 1950 coordinates for peaks of detected radio sources; [Col. 6] angular distance between the IRAS and the radio sources in seconds of arc; [Cols. 7–9] observed source peak size (major and minor axis in seconds of arc), and position angle from N to E in degrees; [Cols. 10–12] beam-deconvolved size parameters; [Col. 13] halo size in seconds of arc, when an extended component is detected above the 2σ level; [Col. 14] morphological class after WC89 (see also Sect. 3.3); [Col. 15] peak flux density in mJy/beam; [Col. 16] integrated flux density in mJy; [Col. 17] image r.m.s. in mJy/beam.

The set of observational parameters obtained for each source after the higher resolution image has been degraded to the resolution of the other (lower resolution) image is given in parentheses; one source (#37) was visible at 2 cm only after degrading the image, so only values in parentheses are given. It must be emphasized that not all radio-detected sources are believed to be associated with the corresponding IRAS source. A criterion for establishing a real association is discussed in Sect. 3.3: here, we anticipate that the association rates are 43% and 24% for *High* and *Low* sources, respectively.

3.1. Derivation of physical parameters

We will assume that the origin of the radio emission from our sources is optically thin thermal bremsstrahlung arising in an ionised circumstellar environment. For compact or unresolved sources the electron density, emission measure, ionised hydrogen mass and photon density of the Lyman continuum were derived using the formulae of Mezger & Henderson (1967) with the refinements of Panagia & Walmsley (1978). This formalism is suitable for spherical sources, but it was also adopted for non-spherical ones provided that they did not show complex structures or extended halos; in these cases we took the geometric average of the two axes as a representative size for the radio source. Source geometry is in any case poorly known and therefore any attempt to refine the model taking geometry into account would not provide more accurate results.

For extended or multicomponent sources, peak properties were derived following WC89. The beam brightness temperature is estimated from:

$$T_{\rm b} = \frac{S_\nu 10^{-26} c^2}{2\nu^2 k \Omega_{\rm b}} \qquad [{\rm K}] \tag{1}$$

where S_ν is the peak flux density in mJy/beam, c is the speed of light in cm/s, ν is the frequency in Hz, and $\Omega_{\rm b}$ is the beam solid angle. If the ionised gas is at a temperature $T_{\rm e}$, the optical depth is given by

$$\tau = -\ln\left(1 - \frac{T_{\rm b}}{T_{\rm e}}\right) \tag{2}$$

The emission measure EM is given by:

$$EM = \frac{\tau}{8.235 \cdot 10^{-2} \alpha T_{\rm e}^{-1.35} \nu^{-2.1}} \qquad [{\rm pc\ cm^{-6}}] \tag{3}$$

where α (which depends on the frequency and electron temperature) is a correction factor $\sim$1 and the frequency is expressed in GHz. In the following we assume $T_{\rm e} = 10^4$ K. The electron density is given by:

$$n_{\rm e} = \sqrt{\frac{EM}{\Delta s}} \qquad [{\rm cm^{-3}}] \tag{4}$$

where Δs is the optical path length through the peak and is defined as the geometrical mean of the two axes of the source, after having applied Panagia & Walmsley's (1978) correction. For extended or complex sources, as the 3D geometry is unknown, the derived properties are "peak" ones because the peak radio flux density was used in the above formulae and the mass of ionised hydrogen was computed multiplying the peak electron density by the proton mass and by the volume of the emitting region.
The photon flux of the Lyman continuum is independent of the source geometry and has been estimated using integrated properties. It is given by Mezger & Henderson (1967) as follows:

$$N_{\rm Ly}({\rm s^{-1}}) = 4.76 \cdot 10^{48}\, S_{\rm int} d^2 \nu^{0.1} T_e^{-0.45} \alpha^{-1} \tag{5}$$

where $S_{\rm int}$ is the integrated flux density in Jy, d is the distance in kpc, ν is in GHz, and $\alpha \simeq 1$ (see before).
The spectral index α_ν is defined as $S_\nu \propto \nu^{-\alpha_\nu}$. Hence,

$$\alpha_\nu = \frac{{\rm Log}\, S_2 - {\rm Log}\, S_6}{{\rm Log}\, 6 - {\rm Log}\, 2} \tag{6}$$

where S_2 and S_6 are the integrated flux densities at 2 and 6 cm, respectively. However, the determination of the spectral index is only indicative because the $u-v$ plane has been sampled differently at the two wavelengths. As already mentioned (Sect. 2.4, this problem is not solved by simply degrading the higher resolution image, but rather one should exclude the short baselines in the low-resolution configuration. This implies a substantial reduction of visibilities leading to a reduction in sensitivity. As the observations at 2 cm are in general less sensitive to extended emission than those at 6 cm, the spectral index should be considered a lower limit for extended sources. In cases where 2 cm

Table 1. a *High* sources at 6 cm[†]

(1) Mol#♣	(2) λ (cm)	(3) Run	(4) Peak pos. α(1950)	(5) δ(1950)	(6) Δ ($''$)	(7) Core parameters Observed maj ($''$)	(8) min ($''$)	(9) P.A. (°)	(10) Deconvolved maj ($''$)	(11) min ($''$)	(12) P.A. (°)	(13) Halo ($''$ x $''$)	(14) MC◇	(15) Observed fluxes Peak (mJy/beam)	(16) Integ. (mJy)	(17) rms♡ (mJy/beam)
7	6	II	No detection													
9	6	II	05:17:00.961	+36:35:17.96	102	6.85	1.77	−64.2	2.02	0.44	97.0		S	2.50	4.23	0.07
10	6	II	No detection													
74[e]	6	II	18:50:46.663	+01:21:01.82	23	5.66	1.99	63.3	0.85	0.66	40.2		S	8.57	12.24	0.10
76[t]	6	II	No detection													
78[h] N	6	II	18:53:18.284	+00:47:29.31	8	5.99	2.85	63.4	2.34	2.01	119.7		S	7.49	14.91	0.07
S	6	II	18:53:18.542	+00:47:21.80	12	5.93	2.00	61.5	1.94	0.97	56.6		S	1.89	2.41	0.07
81	6	II	18:55:11.702	+03:02:01.16	2	6.60	2.45	66.1	3.40	0.97	74.3		S	28.39	39.97	0.30
93 S1	6	II	19:04:22.988	+07:26:57.32	11	4.00	1.99	69.5	2.85	1.71	78.7	20x20	CH	6.01	45.02	0.19
S3	6		19:04:22.972	+07:26:53.66		−[‡]	−	−	−	−	−			3.90		
S4	6		19:04:22.420	+07:26:50.20		9.68	3.01	62.7	7.84	2.47	62.4			1.25		
S5	6		19:04:23.211	+07:26:51.94		−	−	−	−	−	−			1.95		
N1	6		19:04:23.273	+07:27:06.62		12.92	4.57	65.5	11.61	4.22	66.1	15x15	CH	1.88	15.58	
N2	6		19:04:23.096	+07:27:08.57		14.75	5.77	44.6	13.74	5.19	41.5			1.71		
97	6	II	19:08:53.426	+09:02:27.37	17	6.27	1.06	63.2	unresolved				S	11.52	10.78	0.39
99	6	II	19:09:35.829	+09:42:48.58	150[a]	5.66	1.98	63.6	unresolved				S	2.61	5.68	0.09
102	6	II	19:19:50.281	+14:23:30.09	4	5.53	2.45	62.0	2.03	1.28	175.5		S	2.17	2.86	0.16
103 C1	6	II	19:21:23.250	+17:23:16.51	9	9.72	5.07	72.6	7.95	4.64	79.7	30x30	I	24.77	496.25	0.49
C2	6		19:21:23.297	+17:23:12.73		14.86	5.34	70.3	13.74	5.03	71.7			15.87		
C3	6		19:21:23.011	+17:23:05.43		9.44	8.07	-62.0	9.04	6.09	137.6			11.33		
C4	6		19:21:23.519	+17:23:07.76		13.50	4.59	76.0	12.31	4.05	78.9			11.19		
C5	6		19:21:22.728	+17:23:22.25		12.70	4.37	68.9	11.35	4.00	70.6			7.63		
C6	6		19:21:23.098	+17:23:28.87		10.94	3.45	53.9	9.37	2.88	50.7			4.24		
104	6	II	No detection													
108	6	II	No detection													
109	6	II	19:37:27.843	+23:52:51.60	21	5.39	1.80	63.0	0.85	0.65	24.8		S	64.40	72.53	0.05
110[g]	6	II	19:38:52.341	+23:57:41.73	7	5.37	1.76	63.6	0.80	0.46	73.1		S	2.11	2.96	0.06
114 N	6	II	20:04:55.746	+27:21:39.33	124[b]	5.18	1.81	64.3	1.29	0.60	32.7		S	2.93	4.05	0.03
S	6	II	20:04:55.790	+27:21:34.61	128	5.89	1.89	70.4	3.11	0.68	82.5		S	0.61	1.03	0.03
115	6	II	No detection													
116	6	II	No detection													
119	6	II	No detection													
121[m] N	6	II	20:18:50.928	+39:28:38.81	1	5.04	1.79	65.0	1.16	0.64	77.2		S	2.86	3.82	0.08
S	6	II	20:18:50.692	+39:28:17.07	21	5.02	2.04	64.4	1.19	1.02	159.0		S	21.19	29.95	0.08
123[d] C1	6	II	20:22:03.064	+37:28:27.54	7	10.25	4.87	85.5	9.13	4.11	92.4	20x20	I	48.18	458.09	0.55
C2	6		20:22:02.923	+37:28:22.33		8.92	5.86	80.9	7.58	5.30	93.9			31.04		
C3	6		20:22:03.250	+37:28:25.05		9.89	7.37	65.6	8.49	7.17	67.5			30.32		
126	6	II	No detection													
131	6	II	20:44:27.483	+46:29:37.74	1	4.86	1.72	63.8	unresolved				S	2.15	2.88	0.06
133[f]	6	II	21:07:45.464	+52:10:47.68	60[c]	12.33	7.65	0.8	11.46	6.16	0.8	60x45	CH	7.39	263.72	0.44
138	6	II	No detection													
139	6	II	No detection													
145	6	II	No detection													
148	6	II	No detection													
151	6	II	22:50:32.797	+59:42:50.11	136	4.02	1.66	71.6	unresolved				S	7.19	8.04	0.09

♣ underlined and bold-face indicates association with the IRAS source.
◇ see Sect. 3.3 for an explanation of the lettering used.
♡ see Sect. 2 for the image *rms* in non-detected sources fields.
† Following sources were not detected in the present survey, but detected by others:
104 - KCW94 at 3.6cm ($F_{\rm int}$=1.5 mJy) - VLA (B);
119 - HML94 at 6cm ($F_{\rm int}$=0.85 mJy) - VLA (C) - double $t_{\rm int}$ compared to us;
126 - McCutcheon et al. 1991 at 6cm ($F_{\rm int}$=108mJy) - VLA (C) - source is very extended ($97''$x$40''$) so possibly too faint for us;
[a] radio peak is $15''$from PSC source IRAS19095+0942.
[b] radio peaks are $\sim 24''$from PSC source IRAS20049+2721.
[c] as radio source is extended association is considered positive; the other PSC source IRAS21078+5209 is $87''$away and hence is not considered associated.
[d] Source 123 detected by KCW94 at 2cm ($F_{\rm int}$=67.6 mJy) and 3.6cm ($F_{\rm int}$=109.1 mJy) with the VLA in B configuration;
also detected by Miralles et al. 1994 at 2 and 6cm (with fluxes 347 and 362 mJy respectively) with the VLA in configuration D;
also detected by HML94 at 6cm ($F_{\rm int}$=446.83 mJy) with VLA in conf. C.
[e] Source 74 detected by Miralles et al. 1994 at 2 and 6cm (with fluxes of 9.9 and 9.1 mJy respectively) with the VLA in configuration D;
also detected by HML94 at 6cm ($F_{\rm int}$=8.58 mJy) with VLA in conf. C.
[f] Source 133 detected by Miralles et al. 1994 at 2 and 6cm (with fluxes of 31 and 40 mJy respectively) with the VLA in configuration D.
[g] Source 110 detected by HML94 at 6cm ($F_{\rm int}$=2.21 mJy) with VLA in conf. C.
[h] Source 78 detected by HML94 at 6cm ($F_{\rm int}$=15.79 mJy) with VLA in conf. C.
[t] Source 76 also undetected by McCutcheon et al. 1991 at 6cm with VLA in conf. C.
[m] Source 121 detected and resolved by McCutcheon et al. 1991 at 6cm ($F_{\rm int}$=29 mJy) with VLA in conf. C.
[‡] dashes under col.[7-12] mean that 2D gaussian fit of multiply peaked sources did not converge to meaningful sizes; peak fluxes are correct though.

emission was not detected, the spectral index is not simply an upper limit because it cannot be excluded that a flux even higher than that observed at 6 cm might have been detected with a $u-v$ sampling similar to that of the 6 cm observations. In such cases the spectral index is undetermined.

The derived physical parameters are listed in Tables 2a and b for *High* and *Low* sources respectively. The tables are organised as follows: [Col. 1] running number and identification code as in Tables 1; [Col. 2] wavelength in centimeters; [Col. 3] peak diameter in pc; [Col. 4] halo diameter in pc obtained as a mean of the dimensions in seconds of arc from Tables 1; [Col. 5] brightness temperature; [Col. 6] optical depth; [Col. 7] electron density; [Col. 8] emission measure; [Col. 9] mass of ionised hydrogen; [Col. 10] decimal logarithm of Lyman photon flux; [Col. 11] spectral index (for Table 2b only); [Col. 12] ratio of integrated and peak flux densities.

3.2. Association between IRAS and radio sources

The association of a radio emission peak with the corresponding IRAS source is established on the basis of their separation: for example, some authors (see WC89; Hughes & McLeod 1994, hereafter HML94) assume $1'$ as the maximum separation for a reliable association. For our objects, based on the previous NH_3 observations (Paper I), an improved criterion can be set. Ammonia observations were performed with a beam of $40''$, but, as no mapping was made, it is assumed that the exact location of the molecular peak is known with an uncertainty equal to the beam size. This assumption seems quite reasonable, as the beam size used in our ammonia observations is comparable to the average angular size of moderate- and high-mass ammonia cores (Harju et al. 1993) at a distance of 4 kpc, the typical distance of our sources (see Paper I). Hence, it is assumed that a radio source is associated with the IRAS source if their displacement

Table 1. b *Low* sources at 2 and 6 cm

(1) Mol#♣		(2) λ (cm)	(3) Run	(4) Peak pos. α(1950)	(5) δ(1950)	(6) Δ ($''$)	(7) Core parameters[a] Observed maj ($''$)	(8) min ($''$)	(9) P.A. (°)	(10) Deconvoluted maj ($''$)	(11) min ($''$)	(12) P.A. (°)	(13) Halo ($''$ x $''$)	(14) MC◇	(15) Observed fluxes[a] Peak (mJy/beam)	(16) Integ. (mJy)	(17) rms♡ (mJy/beam)
3		6	I	No detection													
		2	I	No detection													
8		6	I	No detection													
		2	I	No detection													
11		6	II	05:34:26.775	+31:58:30.73	90	7.09	1.75	−63.6	3.05	0.72	117.0		S	10.65	14.27	0.04
		2	III												≤1.35		
12		6	I	No detection													
		2	I	No detection													
28		6	I	No detection													
		2	I	No detection													
30		6	I	17:45:01.681	−27:44:24.41	123	2.72	1.10	5.1		unresolved			S	2.82	2.68	0.09
		2	I												≤1.06		
36		6	I	No detection													
		2	I	No detection													
37		6	I	18:01:48.615	−24:26:51.28	15	2.60	1.16	9.1		unresolved			S	4.90	4.97	0.07
		2	I	18:01:48.622	−24:26:51.11		(2.45)	(1.11)	(8.0)		(unresolved)				(6.75)	(6.99)	(0.16)
38		6	I	No detection													
		2	I	No detection													
39		6	I	No detection													
		2	I	No detection													
45		6	I	18:14:27.218	−17:24:48.50	93	3.97	2.63	22.0	3.25	2.32	28.5		S	4.64	16.83	0.06
							(8.02)	(3.00)	(53.7)	(2.60)	(2.09)	(2.1)			(8.80)	(15.75)	(0.07)
		2	III	18:14:27.225	−17:24:47.89		7.87	2.01	54.7	1.83	0.93	52.9			8.95	10.60	0.21
50		6	I	18:16:13.908	−16:12:46.01	10	2.58	1.45	20.5	1.10	0.62	40.6	10x10	CH	2.83	14.63	0.09
							(10.87)	(5.25)	(55.0)	(5.57)	(1.57)	(57.9)			(3.86)	(10.34)	(0.11)
		2	III	18:16:13.889	−16:12:45.68		9.83	1.79	54.5	3.05	0.44	58.6			6.77	10.17	0.14
57		6	I	18:25:45.668	−07:44:43.64	185	1.97	1.35	16.5	0.39	0.31	0.5		S	3.13	4.06	0.04
		2	I												≤1.13		
59		6	I	No detection													
		2	I	No detection													
60		6	I	18:28:49.739	−01:57:18.76	88	1.90	1.43	20.9	0.47	0.17	11.0		S	5.35	4.88	0.04
		2	I	18:28:49.745	−01:57:18.66		(1.71)	(1.31)	(13.4)		(unresolved)				(6.91)	(5.68)	(0.31)
66		6	I	No detection													
		2	I	No detection													
68[e]		6	I	18:39:38.205	−04:31:38.07	24	3.06	1.91	37.0	1.88	1.32	37.4	15x15	CH	2.76	26.62	0.08
		2	I												≤1.05		
70		6	I	18:42:22.558	−03:31:35.96	106	2.39	1.44	33.0	0.72	0.39	31.9		S	6.53	8.81	0.08
		2	I												≤1.06		
75		6	I	18:51:05.719	+01:44:15.67	145	2.28	1.46	35.1	0.73	0.11	15.3		S	3.67	4.18	0.04
		2														not in field	
77		6	I	No detection													
		2	I	No detection													
82		6	I	18:56:34.406	+03:49:28.32	17	2.40	1.57	47.7	0.64	0.36	170.7		S	2.90	3.55	0.06
							(6.53)	(1.90)	(60.3)		(unresolved)				(2.95)	(3.35)	(0.07)
		2	III	18:56:34.315	+03:49:27.33		6.69	1.80	60.2	0.79	0.19	30.7			5.88	6.48	0.14
84		6	I	18:56:48.286	+07:00:38.18	8	2.31	1.59	48.7	0.61	0.29	5.9		S	1.80	2.73	0.06
							(7.28)	(1.79)	(58.7)		(unresolved)				(1.76)	(1.99)	(0.06)
		2	III	18:56:48.320	+07:00:37.87		7.82	1.79	59.6		unresolved				6.34	6.92	0.16
86		6	I	18:57:13.654	+03:49:26.15	46	3.17	1.71	49.1	1.27	0.53	19.1		S	2.87	5.62	0.08
		2	I												≤1.06		
87		6	II	18:58:42.711	+01:06:40.74	71	12.47	4.53	71.0	11.1	4.03	73.7		S	6.89	34.75	0.16
		2	I												≤1.05		
91[f]	C1	6	II	19:01:18.888	+05:05:22.25	51[b]	6.74	1.95	61.9	3.61	0.86	59.4	50x50	I	1.97	48.38	0.09
	C2	6		19:01:18.945	+05:05:28.72		7.93	2.51	71.8	5.64	1.36	80.5			0.78		
	C3	6		19:01:18.505	+05:05:28.63		7.49	2.62	68.8	4.95	1.75	77.1			0.73		
	C4	6		19:01:18.323	+05:05:36.04		6.51	2.75	58.4	3.31	1.87	39.3			0.63		
	C5	6		19:01:19.966	+05:05:27.34		7.74	1.92	64.7	5.25	0.81	64.6			0.67		
		2	I												≤0.96		
98		6	I	19:09:18.172	+08:42:51.07	110	3.46	1.50	58.4		unresolved			S	2.74	3.82	0.08
		2	I												≤1.04		
117[d]	C1	6	II	20:09:54.820	+36:40:36.58	5	7.93	3.97	88.9	6.65	2.85	101.2	25x25	I	2.62	37.38	0.06
	C2	6		20:09:54.783	+36:40:37.44		6.10	4.16	48.0	4.50	2.80	9.9			2.55		
	C3	6		20:09:54.700	+36:40:34.17		7.35	2.96	62.3	5.53	2.40	59.4			2.10		
	C4	6		20:09:55.112	+36:40:34.53		6.98	2.57	65.2	5.02	1.95	64.7			1.58		
	C5	6		20:09:55.062	+36:40:31.87		8.55	3.17	64.9	7.04	2.68	64.4			1.21		
	C6	6		20:09:55.084	+36:40:28.16		6.98	2.50	73.6	5.08	1.64	80.6			0.79		
	C7	6		20:09:54.731	+36:40:29.10		10.07	5.58	60.4	8.84	5.30	58.2			0.92		
	C8	6		20:09:54.253	+36:40:37.69		7.37	4.48	78.1	5.73	3.90	92.7			0.92		
	C9	6		20:09:54.274	+36:40:42.95		8.86	3.03	64.5	7.41	2.52	64.0			0.79		
	C10	6		20:09:54.651	+36:40:40.28		6.46	5.63	−53.9	6.09	3.14	146.5			1.07		
	C11	6		20:09:54.583	+36:40:24.19		6.91	1.84	65.1	3.96	0.91	67.8			0.87		
	C1/3	2	III	20:09:54.900	+36:40:35.67		4.89	1.65	63.0	1.10	0.47	61.2	25x15		6.10	16.52	0.08
	C2/4	2		20:09:54.736	+36:40:38.62		5.39	1.74	64.5	2.52	0.69	69.1			1.39		
	C8/10	2		20:09:54.469	+36:40:39.52		6.19	1.84	65.1	3.96	0.91	67.8			0.87		
118		6	I	No detection													
		2	I	No detection													
122		6	I	No detection													
		2	I	No detection													
125		6	I	No detection													
		2	I	No detection													
129[c]		6	II	20:33:19.293	+41:02:43.16	25	10.08	8.97	−83.4	8.87	7.59	96.5	80x45	I	7.11	490.32	0.67
		2	III	20:33:18.928	+41:02:36.89		5.00	1.71	63.4	1.74	0.54	72.3	30x30		6.95	(91.86)	0.10
136		6	I	21:30:55.315	+50:49:54.36	92	1.88	1.18	−87.1	0.44	0.13	60.3		S	13.95	14.19	0.08
							(4.17)	(1.64)	(63.3)	(0.28)	(0.02)	(93.5)			(14.32)	(14.59)	(0.04)
		2	III	21:30:55.315	+50:49:54.42		4.14	1.66	63.7		unresolved				6.13	7.27	0.19
143		6	I	No detection													
		2	I	No detection													
154		6	I	No detection													
		2	I	No detection													
155	N	6	II	23:14:01.014	+61:22:49.37	87	4.42	2.02	78.2	1.93	0.80	96.1		S	5.23	10.91	0.07
		2	III	23:14:00.981	+61:22:49.22		4.49	1.65	74.0		unresolved				1.27	2.68	0.19
							(4.90)	(1.67)	(74.1)		(unresolved)				(1.21)	(2.25)	(0.15)
155	S1	6	II	23:14:01.931	+61:21:25.74	9	6.36	2.27	73.9	4.93	1.43	73.7	15x10	I	1.26	12.68	0.07
	S2	6		23:14:01.615	+61:21:27.52		5.66	2.13	75.1	3.99	1.20	75.9			1.15		
	S3	6		23:14:01.340	+61:21:29.93		6.32	2.15	75.0	4.88	1.23	75.4			0.76		
		2	III	23:14:01.737	+61:21:27.11		3.82	1.75	70.2	1.11	0.34	82.7			5.68	8.75	0.19
							(4.15)	(1.79)	(74.7)	(1.07)	(0.29)	(79.5)			(5.57)	(7.64)	(0.15)
158		6	I	No detection													
		2	I	No detection													
160		6	I	No detection													
		2	I	No detection													

♣ underlined and bold-face indicates association with the IRAS source.
◇ see Sect. 3.3 for an explanation of the lettering used.
♡ see Sect. 2 for the image *rms* in non-detected sources fields.
[a] numbers in parantheses indicate values obtained after spatial smoothing (see text).
[b] considering source extension this association is considered as positive.
[c] 6 and 2 centimeters maps have been reconstructed with a circular $48''$ beam;
Source 129 also detected at 2 and 6cm by Miralles et al. 1994 (with fluxes 43 and 42 mJy respectively) with the VLA in configuration D.
[d] Source 117 also detected at 6cm by HML94 (F_{int}=36.92 mJy) with VLA in conf. C.
[e] Source 68 also detected at 6cm by HML94 (F_{int}=20.85 mJy) with VLA in conf. C.
[f] Source 91 also detected at 6cm by HML94 (F_{int}=83.76 mJy) with VLA in conf. C.

Table 2. a Physical parameters derived for *High* sources at 6 cm

(1) Mol# ♣		(2) λ (cm)	(3) Φ core (pc)	(4) Φ halo (pc)	(5) T_b (K)	(6) τ (10^{-3})	(7) n_e (10^4 cm^{-3})	(8) EM (10^6 pc cm^{-6})	(9) M(HII) (10^{-3} $M_\odot$)	(10) Log N_{Ly} (s^{-1})	(12) F_{int}/F_{peak}
9		6	0.053				0.49	0.91	7.88	46.36	1.69
74		6	0.07				0.34	0.60	13.1	46.21	1.43
78	N	6	0.076				0.34	0.65	16.8	46.53	1.99
	S	6	0.049				0.27	0.25	3.47	45.74	1.28
81		6	0.064				0.72	2.44	21.2	46.74	1.41
93[a]		6	0.077	0.42	116.1	12	0.37	1.05	19.5	46.60	8.29
93[b]		6	0.25	0.32	10.5	1	0.06	0.09	113	46.14	7.49
97		6	≤0.11				≥0.20	≥0.31	≤30.0	46.33	0.94
99		6	≤0.19				≥0.08	≥0.10	≤61.8	46.49	2.18
102		6	0.08				0.19	0.22	11.1	45.89	1.32
103[c]		6	0.21	0.60	120.3	12	0.23	1.0	256	48.08	20.03
109		6	0.029				3.43	25.1	9.61	47.08	1.13
110		6	0.024				0.94	1.54	1.41	45.68	1.40
114	N	6	0.006				1.53	1.00	0.035	44.50	1.38
	S	6	0.0095				0.38	0.098	0.036	43.90	1.69
121	N	6	0.0025				2.35	0.98	0.004	43.73	1.34
	S	6	0.003				4.63	48.2	0.015	44.62	1.41
123[a]		6	0.23	0.44	219.4	22	0.30	2.00	439	47.92	9.51
131		6	≤0.064				≥0.12	≥0.07	≤3.49	45.18	1.34
133		6	0.095	0.37	19.9	2	0.14	0.18	14.4	46.85	35.69
151		6	≤0.14				≥0.15	≥0.23	≤41.9	46.58	1.12
Median			0.064±0.019				0.37±0.35	0.98±3.21	11.1±30.6	46.33±0.26	1.41±2.00
Average			0.078±0.019				0.98±0.32	5.08±3.05	54.5±28.6	46.05±0.25	4.96±1.83

♣ underlined and bold-face indicates association with the IRAS source.
[a] refers to component S1.
[b] refers to component N1.
[c] refers to component C1.

Table 2. b Physical parameters derived for *Low* sources at 6 and 2 cm

(1) Mol# ♣		(2) λ (cm)	(3) Φ core (pc)	(4) Φ halo (pc)	(5) T_b (K)	(6) τ (10^{-3})	(7) n_e (10^4 cm^{-3})	(8) EM (10^6 pc cm^{-6})	(9) M(HII) (10^{-3} $M_\odot$)	(10) Log N_{Ly} (s^{-1})	(11) F_{int}/F_{peak}	(12) α_ν
11		6	0.024				0.86	1.30	1.32	45.83	1.34	–
30[a]		6	≤0.032				≥0.26	≥0.16	≤1.02	45.19	0.95	–
37		6	≤0.025				≥0.40	≥0.29	≤0.68	45.46	–	0.31
		2	≤0.024				≥0.54	≥0.40	≤0.81	45.41	–	
45		6	0.092				0.30	0.61	25.60	46.66	1.79	−0.36
			(0.090)				(0.30)	(0.59)	(24.10)	(46.63)		
		2	0.052				0.61	1.07	9.20	46.52	1.18	
50		6	0.02	0.24	52.1	5	0.36	0.47	0.35	46.49	2.68	−0.02
			(0.07)	(0.24)	(13.2)	(1)	(0.10)	(0.12)	(4.12)	(46.06)		
		2	0.027		2.6	0.2	0.21	0.24	0.50	46.11	1.50	
57		6	0.009				3.09	6.43	0.27	45.70	1.30	–
60		6	0.001				11.0	11.7	0.003	44.27	0.91	0.14
		2	≤0.008				≥0.93	≥0.37	≤0.045	44.39	0.82	
68		6	0.046	0.44	45.8	4.6	0.23	0.41	2.69	47.27	9.68	–
70		6	0.016				22.7	5.87	1.1	46.17	1.35	–
75		6	0.010				3.69	9.96	0.42	45.96	1.14	–
82		6	0.030				1.17	2.95	3.43	46.16	1.14	0.60
			(≤0.20)				(≥0.06)	(≥0.06)	(≤63.1)	(46.35)		
		2	0.024				2.17	8.26	3.36	46.64	1.10	
84		6	0.008				2.21	2.95	0.14	45.06	1.13	1.13
			(≤0.07)				(≥0.08)	(≥0.03)	(≤3.17)	(45.13)		
		2	≤0.07				≥0.14	≥0.08	≤6.31	45.73	–	
86		6	0.030				0.89	1.65	2.35	46.09	1.96	–
87		6	0.14				0.15	0.22	41.6	46.57	5.04	–
91[b]		6	0.045	0.70	11.0	1	0.15	0.10	1.64	46.56	24.56	–
98		6	≤0.094				≥0.15	≥0.14	≤13.0	46.05	1.39	–
117[b]		6	0.32	1.05	17.7	2	0.07	0.16	276	47.40	14.27	−0.74
117[c]		2	0.057	0.81	4.6	0.5	0.27	0.42	6.01	46.81	3.37	
129[a]		6	0.13	0.58	17.1	2	0.11	0.15	29	46.95	68.96	−1.52
		2	0.018	0.29	51.2	5	0.50	0.46	0.35	46.23	13.22	
136		6	0.011				7.76	47.5	1.1	46.70	1.02	−0.63
			(0.003)				(45.0)	(49.9)	(0.19)	(46.71)		
		2	≤0.12				≥0.16	≥0.18	≤30.1	46.47	–	
155	N	6	0.07				0.53	1.44	21.0	46.82	2.09	−1.44
		2	≤0.15				≥0.09	≥0.07	≤33.3	46.26		
			(≤0.16)				(≥0.08)	(≥0.05)	(≤33.4)	46.19	–	
155	S1	6	0.14	0.38	9.9	1	0.08	0.09	26.4	46.42	10.06	−0.46
		2	0.036				1.38	3.91	7.33	46.78	1.37	
			(0.033)				(1.5)	(4.15)	(5.92)	(46.72)		
Median			0.03±0.02				0.86±1.45	1.44±2.78	2.35±16.0	46.17±0.17	1.79±3.75	
Average			0.063±0.019				3.07±1.35	5.22±2.62	24.13±15.0	46.18±0.17	7.64±3.5	

♣ underlined and bold-face indicates association with the IRAS source
[a] a 2 kpc distance has been assumed.
[b] refers to component C1.
[c] refers to component C1+C3.

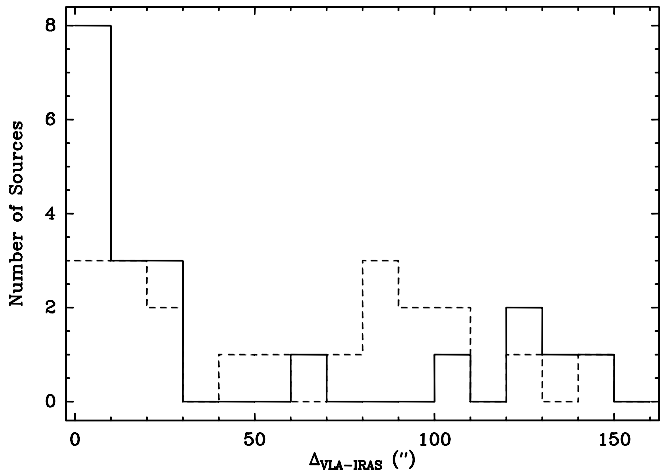

Fig. 1. Histogram of the distribution of sources with respect to the angular separation Δ between radio peaks and IRAS sources. Full and dashed lines represent *High* and *Low* sources respectively. In case of complex sources exhibiting multiple radio peaks embedded in the same diffuse emission, only the brightest peak has been considered (#93, 103 and 123 in the *High* group, and #91, 117 and 155S in the *Low* group).

Table 3. Radio continuum and H_2O properties of the *High* and *Low* samples

Radio	H_2O maser	*Low*	*High*
No	No	18	4
No	Yes	10	13
Yes	Yes	0	7
Yes	No	9	6

Δ is $\leq 40''$; for extended radio sources Δ has been taken as the distance between the IRAS source and the edge of the halo.

To show that the choice of $40''$ as the limit for association is indeed appropriate, we show in Fig. 1 the distribution of *High* and *Low* sources with respect to the distance Δ between the radio and IRAS peaks. *High* sources show a more peaked distribution around $\Delta \simeq 0$ than *Low* sources. The arithmetic mean and the median of Δ are $42\farcs3$ and $12\farcs2$ for *High*, and $66\farcs4$ and $51\farcs4$ for *Low* sources. Interestingly, the value of $40''$ corresponds almost exactly to the first minimum value of the distributions both for *High* and *Low* sources. Should one adopt a threshold to establish the association between radio and IRAS peaks with the help of Fig. 1, the value corresponding to the first drop in the distribution would indeed be the most reasonable choice. This threshold value for the association of radio counterparts to IRAS sources is also compatible with the one obtained by Kurtz et al. (1994; hereafter KCW94).

Once the association of radio counterparts with IRAS sources has been established, it is interesting to compare the radio continuum association rates and the H_2O maser detection rates between *High* and *Low* with the help of Table 3.

According to the evolutionary scenario, we should expect that the radio continuum emission characterizes only the latest phases, whereas water emission should be found in younger objects. The results of Table 3 show that 28 of 37 *Low* sources (76%) do not have radio emission, whereas this fraction is reduced to 57% (17/30) for *High* sources. This appears to support the idea that *Low* sources evolve into *High* sources.

Table 4. Morphological classes for IRAS-radio sources. In parenthesis is the number of sources of each type

Sources	Total	S	C	CH	Sh	I
HIGH	16	70%(11)		20%(3)		10%(2)
LOW	9	35%(3)		20%(2)		45%(4)
HIGH+LOW	25	55%(14)		20%(5)		25%(6)
WC89	75	43%	20%	16%	4%	7%
KCW94	72	55%	16%	9%	1%	19%

3.3. Morphology of radio peaks

The radio maps obtained with the procedure described in Sect. 2.4 for all sources are shown in the Appendix. Morphological classes were assigned according to the classification scheme presented by WC89. From column 14 in Tables 1a and b one can see that only objects of class S (spherical or unresolved), CH (core+halo) and I (irregular or multiply-peaked) are found both in *High* and *Low*; the present sample is lacking both "cometary" (C) and "shell" (Sh) sources which had been identified by WC89 in their sample. The percentages of radio sources associated with IRAS sources are summarised in Table 4 together with a comparison with other radio surveys. Note that sources with different radio peaks associated with the same IRAS counterpart have been counted separately. If we also consider radio sources not associated with our IRAS sources, then the overall percentages of *High* and *Low* sources in the three different groups become 75%, 10% and 15% respectively.

The different morphologies are not only an artifact produced by the different spatial resolutions. In fact, multiply-peaked sources are also found among *High* sources, which were observed with a poorer spatial resolution. What could be ascribed to observational effects, is the difference in the average deconvolved dimensions of the 6cm radio peaks: *Low* sources have diameters on average smaller than those of *High* sources and the corresponding median values are 0.025 and 0.053 pc, respectively. This difference, however, is probably not real and may be due to the fact that the configuration of the VLA array was B for *Low* and CnB for *High* sources, resulting in a higher spatial resolution, and hence narrower radio peaks, for *Low* sources.

The percentages of sources belonging to different morphological classes suggest that the compact phase is the longest-lasting phase in the life of an HII region. This result is well known (e.g. WC89) and is probably indicating that the HII region is expanding against an ambient medium which is hotter (~ 100K) and denser (10^7 cm^{-3}) than previously believed (DePree et al. 1995, Akeson & Carlstrom 1996).

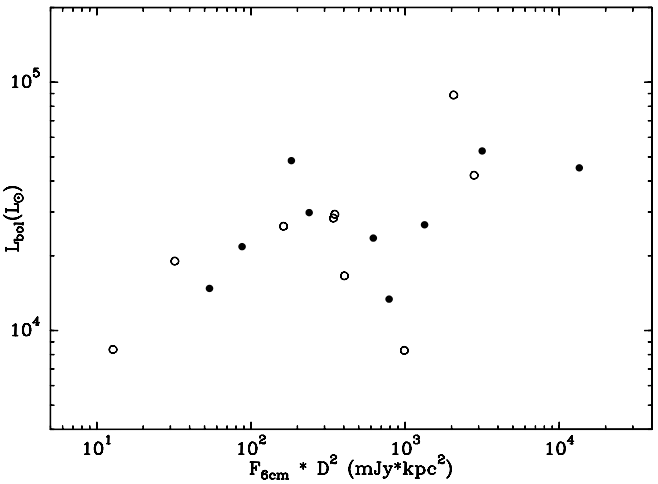

Fig. 2. Plot of the bolometric luminosity as a function of distance-scaled 6 cm flux density. Full and empty circles represent *High* and *Low* detected sources respectively. Note that 4 out of 22 sources are not shown because of unknown distance

4. Discussion

In the following we will discuss separately three groups of sources: IRAS sources associated with a radio peak (the *radio-detected*), IRAS sources not associated with a radio peak (the *radio-non-detected*), and radio peaks not associated with any of the IRAS sources.

4.1. The properties and nature of radio-detected sources

From Tables 2a and 2b one can see that the physical properties of the HII regions associated with the *High* and *Low* sources are very similar. The sole difference concerns the mass of ionised hydrogen which is larger in *High* sources, but this is a consequence of the different dimensions of the regions, which, as noted in Sect. 3.3, can be explained as an observational effect. In fact, the average diameter of *Low* sources is a factor of 1.4 smaller than that of *High* sources, while the ratio of the average masses is 2.4. This is consistent with the scaling of mass with the source diameter that goes like the power 2.5. The similarity between *High* and *Low* sources is also evident in Fig. 2 where the IRAS luminosity is plotted against the distance-scaled 6 cm peak flux density of the corresponding HII region. The two samples represented by filled (*High*) and empty (*Low*) circles are well mixed, so that neither the radio nor the FIR properties may be used to discriminate between *High* and *Low* in this sample. Note that all sources have luminosities between $2\ 10^3$ and $10^5\ L_\odot$, corresponding to exciting stars of spectral type B2 to O7, with the great majority having types earlier than B0.5.

We have just seen that the *High* and *Low* samples are indistinguishable on the basis of their mass, density and emission strength. However, they differ substantially in their "compactness". In order to estimate the "compactness" of continuum emission one can use the ratio of the integrated and peak flux densities: the larger this ratio, the more extended is the HII region. In the case of the IRAS sources with a radio counterpart, the median of the ratio is markedly different for *High* and *Low* sources, 1.5 and 9.9 respectively. A similar result is also found for those radio-detected sources of the survey of HML94 that satisfy the colour criteria of *High* and *Low* sources: in their case the ratio is 1.4 in *High* and 7.7 in *Low* sources. Such a result seems to indicate that *Low* sources detected in the radio continuum are more extended and hence either older than *High* sources, or confined by a less efficient mechanism. This agrees with the conclusion of P91 that part of the *Low* sample may consist of HII regions; however, we stress that these are much less numerous than the radio-non-detected objects, which account for $\sim$75% of the whole *Low* sample.

How do the HII regions found in this study compare with the results of similar previous studies? In Fig. 3 we plot the Lyman continuum luminosity derived from the 6 cm radio flux density against the corresponding bolometric luminosity, $L_{\rm bol}$, estimated from the IRAS data. The *High* and *Low* sources are represented by filled and empty circles respectively, whereas stars indicate the UC HII regions of WC89 and triangles those of KCW94. We also show the theoretical distribution of ZAMS early-type stars (continuous line) according to Panagia (1973), and its location (dashed line) when 90% of the Lyman continuum photons are absorbed by dust. Basically, all sources lie below the continuous line: this is a well-known result which is commonly attributed to three possible causes (see WC89): underestimate of $N_{\rm Ly}$ due to the absorption by dust inside the HII region; overestimate of $L_{\rm bol}$ caused by the fact that IRAS data refer to a region much larger than the HII region itself; overestimate of $L_{\rm bol}$, due to the presence of a cluster containing lower mass, non-ionising stars which contribute only to the IRAS luminosity. All these effects are likely to play a role in explaining the distribution and the spread of the points of Fig. 3.

The main results of Fig. 3 are: (i) the *High* and *Low* sources occupy the same region of the plane, with $L_{\rm bol} < 6\ 10^4\ L_\odot$; (ii) the UC HII regions from WC89 instead have $L_{\rm bol} > 6\ 10^4\ L_\odot$; (iii) the KCW94 UC HII regions cover the whole luminosity range, but at $L_{\rm bol} < 6\ 10^4\ L_\odot$ have Lyman luminosities systematically lower than *High* and *Low* sources. As to the first point, the fact that all of our sources are at lower luminosities than those of WC89 depends on the different colour selection criteria adopted by P91, who selected sources still embedded in compact molecular cores (CMC). Point (ii) reflects the selection effect of the WC89 survey which was performed towards radio continuum peaks, and hence it was strongly biased towards high luminosity stars. On the other hand, KCW94 have observed IRAS point sources selected on the basis of their FIR colours: this explains why their sample is not limited to luminous objects only. Finally, point (iii) is the result of our observations being more sensitive to extended structures than those of KCW94. This is due to the different VLA array configurations and wavelengths used since KCW94 observed in configuration B at 2 and 3.6cm. Also, our sources have a larger distance than those of KCW94 if we consider only those with $L_{\rm bol} < 10^5\ L_\odot$. Therefore, we have recovered a more complete imaging of the extended continuum emission. The difference in

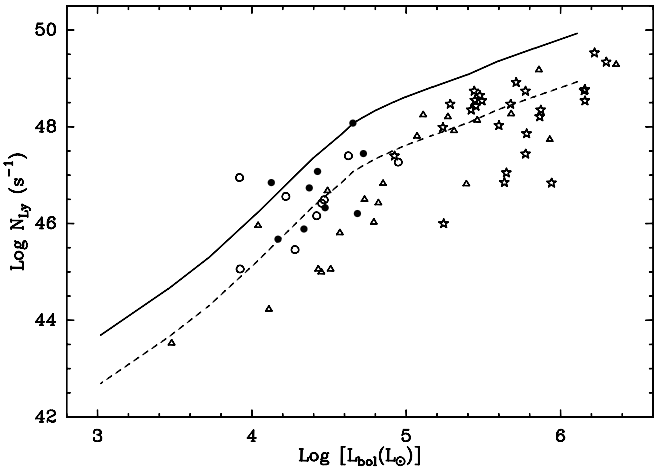

Fig. 3. Plot of the Lyman continuum luminosity (number of Lyman photons per second) as a function of the bolometric luminosity. Full and empty circles indicate radio peaks associated with *High* and *Low* sources respectively. Only sources of known distance are shown. Stars represent sources from WC89 while triangles indicate the sources of KCW94. The full and dashed lines represent the relationships for ZAMS stars (Panagia 1973) with 0% and 90% of Lyman flux absorbed by dust respectively.

distance is explained by the selection criteria of KCW94 who rejected IRAS sources with 100 μm flux less than 1000 Jy.

4.2. The nature of the radio-non-detected sources

As we have just pointed out, an important result of our study is that the frequency of occurrence of *Low* IRAS sources with radio emission is half that of the *High* sources. This result supports our contention that the latter represent a more evolved stage of the evolution of massive stars and that the youngest sources should preferably be found in the *Low* group.

As an alternative possibility, one may imagine that the difference between *High* and *Low* sources is not based on the evolutionary stage, but can be attributed only to a viewing-angle effect if the warm dust responsible for the emission is distributed in a circumstellar disk. In such a case, *High* and *Low* sources would correspond to an edge-on and face-on geometry, respectively, since in the edge-on case the emission would come from the outer and cooler regions of the disk, whereas in the opposite case it is the inner and warmer dust that dominates the emission. As a consequence, *High* sources would have larger [25–12] colours than *Low* sources without being in a different evolutionary phase. Indeed, Yorke et al. (1995) model the spectral energy distribution from luminous, embedded YSOs as a function of the disk viewing angle and it can be seen that the $[25-12]$ colour is significantly affected by the disk orientation. Although attractive, in our opinion this possibility is not completely satisfactory because such a configuration would not account for the different detection rates of radio continuum emission in the two samples observed by us. In the following, we discuss some properties of the radio-non-detected sources that should help clarifying their nature.

First of all, the high fraction of radio-non-detected sources agrees with the recent findings of Cesaroni et al. (1994), Codella & Felli (1995) and Codella et al. (1997) who showed from high-resolution studies of individual star forming regions that water maser spots are positionally coincident with dense cores without continuum emission from ionised gas and switch on prior to the development of an UC HII region. Furthermore it has been shown (Hofner & Churchwell 1996) that also in the presence of cometary UCHII regions the maser spots are often displaced from the apex of the cometary structure and are coincident with hot molecular clumps. Secondly, the bolometric luminosities of the radio-non-detected sources are similar to those of the radio detected ones. Since the luminosity of the exciting stars is high enough ($> 10^4\ L_\odot$) to create an ionised region, we believe that the lack of radio emission in a large percentage of the sources represents an intrinsic property of the sample and it is not the result of a selection bias in favor of low-mass stars. Now, the high infrared luminosity can be due either to a single early-type star or to the cumulative effect of a group/cluster of bright but less massive stars. The latter possibility is quite likely since intermediate-mass stars ($M_* > 8\ M_\odot$) also tend to form not in isolation (see Testi et al. 1997 for a recent study). In such a case, the bolometric luminosity would not be dominated by the single most massive object in the region, but by the contribution of several stars of lower mass. The lack of radio emission would then be explained by the steep mass dependence of the Lyman continuum flux. However, lacking information on the stellar content of our sources, we cannot evaluate the incidence of clusters and test this explanation directly.

Let us now consider the other possibility that the IRAS luminosity is due to a single massive star. We can show that the failure to detect radio emission can be attributed to the compactness of the ionised region, a sign of the extreme youth of the source. To see how, let us consider a spherical, homogeneous, isothermal HII region, with given electron temperature. The peak brightness temperature at a given frequency can be expressed as a function only of its Strömgren radius, $R_{\rm S}$, and of $N_{\rm Ly}$. Once the distance to the source and the HPBW of the telescope are known, it is possible to compute the measured brightness temperature in the synthesised beam, $T_{\rm SB}$, as a function of $R_{\rm S}$ and $N_{\rm Ly}$, and compare it to the upper limits of our observations. In Fig. 4 we plot curves of constant $T_{\rm SB}$ corresponding to these upper limits for a distance of 1 kpc (the corresponding curve for a distance of 5 kpc is shown for comparison as a dashed line). Only points of the $R_{\rm S}$–$N_{\rm Ly}$ plane falling below the curves, which satisfy the condition $T_{\rm SB} \leq T_{\rm SB}[\rm measured]$, are acceptable (i.e. outside of the grey area). Since most sources are between B0.5 and O9, we see from the figure that $R_{\rm S}$ is limited to values below $\sim$400 AU, implying an extremely small and hence young HII region. In principle, the other solution of a radius greater than at least $\sim 10^4$ AU that falls to the right side of the curves in Fig. 4 is also possible, but we tend to exclude it because it would imply unreasonably extended, and hence old objects whereas all the circumstantial evidence accumulated so far (H_2O maser, NH_3 emission, etc.) points to their youth.

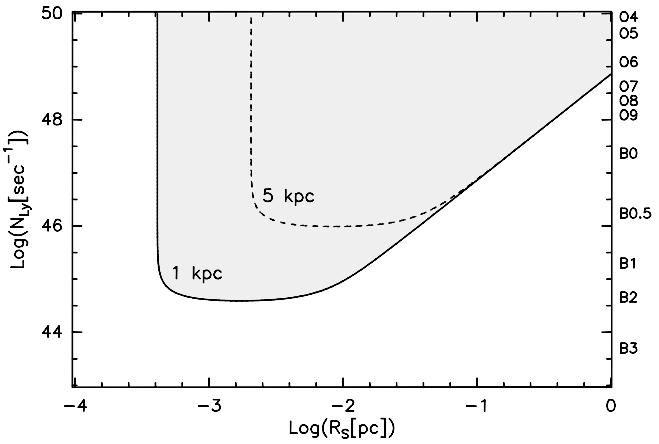

Fig. 4. Curves corresponding to constant values of peak brightness temperature in the synthesised beam, $T_{\rm SB}$(assumed equal to 50K), of a spherical, homogeneous, isothermal HII region. We have assumed an electron temperature of 10000 K and a gaussian beam with HPW of 2″. $R_{\rm S}$ and $N_{\rm Ly}$ are respectively the Strömgren radius of the HII region and the Lyman continuum luminosity of the ionising star (based on the IRAS luminosity); note that $T_{\rm SB}$ is an increasing function of $N_{\rm Ly}$. The labels on the right hand side indicate the values of $N_{\rm Ly}$ corresponding to the spectral types of ZAMS stars (Panagia 1973). The solid line delimits the region where sources can be detected at 1 kpc distance. For sources at $d = 5$ kpc (the maximum distance in our sample), the grey area shrinks as indicated by the dashed line

Pursuing the hypothesis that the non-detected sources are massive extremely young stars, we now briefly consider the physical mechanism responsible for the quenching of the HII region. Much of the recent discussion about young massive stars has been centered around the issue of what maintains an UC HII region in that stage for a time sufficiently long to account for their high frequency of occurrence. Our sample allows us to investigate another important feature of the evolution, namely the physical reason for the inhibition of the development of the ultracompact phase. Given the youth of these sources, the most likely process that controls the evolution is accretion. Indeed the pre-main sequence evolution of a high mass object is very fast (or non existent at all) and the star reaches the ZAMS while still accreting matter (see also Beech & Mitalas 1994). However, if the accretion rate is substantial then the formation of the HII region can be completely inhibited. Following Walmsley (1995), the critical accretion rate can be expressed as:

$$\dot{M}_{\rm inhib} = \sqrt{4\pi N_{\rm Ly}\, G M_\star m_{\rm H}^2 \beta^{-1}} \qquad (7)$$

where $N_{\rm Ly}$ is the Lyman photon flux and β is the hydrogen recombination coefficient ($\sim$4.1·10^{-13} cm^3 s^{-1}). The main parameters for stars of early spectral types are listed in Table 5. We see that for an O8 ZAMS star, corresponding to the brightest sources of our sample, the Lyman photon flux would then require an accretion rate $\sim 2 \cdot 10^{-5}\ M_\odot\,{\rm yr}^{-1}$ to completely choke-off the HII region. On the other hand, if we consider a B0 star, the critical accretion rate decreases to $\sim 4 \cdot 10^{-6}\ M_\odot\,{\rm yr}^{-1}$. Such values of the mass accretion rate are those typically required for the formation of low- and intermediate-mass stars (e.g. Palla & Stahler 1990). Massive protostars are believed to be characterised by even higher values of $\dot{M}_{\rm acc}$, since they are born in clouds with high nonthermal support. Recalling that the average luminosity of our sources corresponds to that of a B0 star, it follows that a relatively modest mass accretion rate can explain the lack of radio emission. It is gratifying to see how an average rate of $\sim 10^{-5}\ M_\odot$ yr^{-1} can control and explain the main properties of protostars up to $\sim 20\ M_\odot$. The distinguishing characteristic of the sources of our sample, both Low and High, is that they are not massive enough to produce an HII region in the presence of residual or main accretion. That is, we are exploring a crucial mass interval where stars begin to copiously produce UV photons: as indicated in Table 5, the mass dependence of the Lyman continuum flux is much steeper than that of the bolometric luminosity (which becomes almost flat for stars more massive than $\sim 20\ M_\odot$). Had we included brighter sources in our sample, the radio detection rate would have been significantly higher, as in the case of the objects studied by WC89. For an O5 star, the value of $\dot{M}_{\rm inhib}$ exceeds $10^{-4}\ M_\odot$ yr^{-1} and, unless the accretion rate becomes very large, it gets easier and easier for the UV photons to break through the infalling gas.

Table 5. Properties of early-type (ZAMS) stars. Lyman continuum photon fluxes, luminosities, and radii are taken from Panagia (1973) for O5 to B3 stars, and Thompson (1984) for B5 and B8; masses are from Schmidt-Kaler (1981). Numbers between parentheses in Cols. 5–7 indicate powers of ten.

Spectral Type	Log($N_{\rm Ly}$) (sec^{-1})	M_* ($M_\odot$)	R_* ($R_\odot$)	L_* ($L_\odot$)	$L_{acc}^{(-5)}$ ($L_\odot$)	$L_{acc}^{(-4)}$ ($L_\odot$)
O5	49.62	60	12.6	6.8(5)	1.5(3)	1.5(4)
O8	48.35	23	6.5	6.5(4)	1.1(3)	1.1(4)
O9	48.08	19	6.0	4.6(4)	1.0(3)	1.0(4)
B0	47.36	18	5.5	2.5(4)	1.0(3)	1.0(4)
B1	45.29	13	4.8	3.2(3)	8.5(2)	8.5(3)
B2	44.65	10	4.3	2.9(3)	7.3(2)	7.3(3)
B3	43.69	7.6	3.4	1.0(3)	7.0(2)	7.0(3)
B5	42.22	5.9	2.7	4.1(2)	6.9(2)	6.9(3)
B8	40.03	3.8	2.2	9.3(1)	5.4(2)	5.4(3)

Although accretion turns out to be dynamically important for the development of the HII region, its impact on the energetics of the star is far less relevant. In the last two columns of Table 5 we give the accretion luminosity for two mass accretion rates, $\dot{M}_{\rm acc} = 10^{-5}$ and $10^{-4}\ M_\odot$ yr^{-1}, respectively. The accretion luminosity has been computed as $L_{\rm acc} = 314\, L_\odot\ (M_*/M_\odot)\ (R_\odot/R_*)\ (\dot{M}_{\rm acc}/10^{-5})$. Comparing these values with L_*, we note that the accretion luminosity (underlined in the table) becomes smaller than the stellar luminosity already at $M_* > 8\, M_\odot$ for $10^{-5}\ M_\odot$ yr^{-1}, and at $M_* > 18\, M_\odot$ for $10^{-4}\ M_\odot$ yr^{-1}. Thus, the accretion luminosity is never energetically dominant and cannot account for the observed IRAS luminosity.

The arguments developed so far are based on the assumption of spherical accretion in which matter falls on the star from

all directions. This assumption is not very realistic because envelope rotation naturally leads to an anisotropic distribution of circumstellar matter and disk formation (cf. Terebey et al. 1984). In these conditions lines of sight exist along which the ionising radiation can escape and produce a detectable HII region despite the fact that accretion still proceeds through the circumstellar disk. However, we will see now that this is not necessarily the case. Let us consider for example the model of photoevaporating disks developed by Hollenbach et al. (1994). The disk is illuminated by central stars with Lyman continuum photon luminosities, $P_{\rm i}$, and weak stellar winds which is more relevant to our case since we sample massive stars of later spectral type. According to the model, the disk extends to a radius $r_{\rm d}$ but the characteristic length is $r_{\rm g}$, the gravitational radius (defined where the sound speed equals the disk escape velocity), which corresponds to $r_{\rm g} = 2 \cdot 10^{15}$ cm for a B0 star. This radius is small compared to the resolution of our VLA observations. Inside $r_{\rm g}$ the disk is surrounded by an atmosphere with scale height larger than the stellar radius: this is important since it means that many UV photons do not necessarily escape freely in space. Now, according to Hollenbach et al. (1994), the rate of photoevaporation of a disk is (cf. their Eq. 3.14)

$$\dot{M}_{\rm dw} \; = \; 1.3 \cdot 10^{-5} \; P_{\rm i}^{1/2} \; (M_*/10 M_\odot)^{1/2} \;\; M_\odot \; {\rm yr}^{-1} \qquad (8)$$

where $P_{\rm i}$ is in units of 10^{49} photons/sec and for a B0 star is approximately 0.04. Thus, the rate of ionised material that escapes from the disk is about $\dot{M}_{\rm dw} \simeq 3 \cdot 10^{-6} \; M_\odot$ yr^{-1}. This material would escape freely if one does not consider that the disk is embedded in the envelope whose material is still infalling toward it. Thus, recalling the magnitude of $\dot{M}_{\rm inhib}$ derived above, we see that $\dot{M}_{\rm dw} < \dot{M}_{\rm inhib}$ and the average $\dot{M} > \dot{M}_{\rm inhib}$. Therefore, a modest mass accretion rate onto the disk can still manage to limit the HII region from the disk itself. Of course, due to the flattening of the disk, there will be some photons that escape and ionise the surrounding gas, but the opening angle is small and the emission measure will hardly be detectable. Of course, these order of magnitude arguments should be made more rigorous (especially considering the complexity of the interaction between accreting matter and the evaporating ionised gas), but it is nevertheless instructive to see how simplified models can naturally explain the lack of radio detection from embedded, luminous IRAS sources.

Finally, we consider the effect of dust within the HII region as another likely source of UV photon absorption. Which dust column density is needed to completely obscure the ionising flux from a B0 ZAMS star? The Lyman flux from such a source is of the order of $4 \cdot 10^{47}$ photons per second. However, as shown in Fig. 3, at luminosities typical of B0 stars our observations have revealed Lyman fluxes down to a factor of one hundred below this value. This requires a dust attenuation factor of the Lyman continuum, $e^{-\tau_{\rm d}} \simeq 100$. Using a typical grain radius of 0.1 μm and an absorption efficiency $\sim$1 at 912 Å (Draine & Lee 1984), this implies a gas column density $N_{\rm H} \simeq 10^{22}$ cm^{-2} (where we have used the standard gas/dust ratio of 100). In Sect. 4.2, we have seen that radio-non-detected HII regions must have a diameter less than 0.004 pc (see Fig. 4), with a corresponding volume density above $8 \cdot 10^5$ cm^{-3}. This is an order of magnitude higher than typical values (e.g. Churchwell 1991) and is consistent with the high density gradient required by the accretion scenario in order to confine the expansion of the ionised gas. It also reinforces the idea that the non-detection in the radio continuum of most of the *Low* sources can be explained by the high density environment in which they are embedded. In a forthcoming paper, we will discuss the properties of the (sub)millimeter dust continuum emission towards the *Low* sources.

4.3. The nature and properties of non-IRAS radio peaks

Finally, we discuss radio peaks not associated with any of the IRAS sources of our sample. Most of the detected sources have no IRAS counterpart at all, and only a few turned out to be associated with IRAS sources not belonging to our sample.

All the radio peaks found in fields centered on the *Low* sources were checked for association either with other PSC sources failing our selection criteria (see Sect. 1) or with diffuse infrared emission which IRAS fails to detect as a point source (in the galactic plane confusion problems play a decisive role). In most cases, we see far-infrared emission from the radio source. The radio peaks generally show physical properties that do not significantly differ from those discussed in Sect. 4.1, indicating that they probably sample the same population of objects. Compact infrared counterparts of these sources should be present, but their identification would require a detailed investigation of the coadded IRAS images, a task which goes beyond the scope of this work.

An alternative explanation is that the radio sources are extragalactic objects. However, their location on the galactic plane does not allow to check association with available catalogues of extragalactic sources. Rodriguez et al. (1989) provide an estimate of the number of extragalactic radio sources which can be expected as a function of the flux and the VLA field of view at 6 cm. Our faintest object has a 6 cm flux density of the order of 1 mJy corresponding to an average of ~ 0.3 extragalactic radio sources in our $5' \times 5'$ field of view. Thus, based on this argument, it is unlikely that the non-IRAS radio peaks are associated with galaxies. On the other hand for few of the non-IRAS radio peaks, namely sources 45, 60, 136, 155N, we could estimate the radio spectral index being -0.36, 0.14, -0.63, -1.44 respectively (see also Table 2b); keeping in mind that these values can be only considered as lower limits (see Sect. 3.1), we regard as a reasonable possibility that at least sources 136 and 155N might be extragalactic objects.

5. Conclusions

To summarise, we seem to identify an evolutive sequence within our sample of observed sources. Sources with a radio counterpart can be best explained as ZAMS stars where moderate amounts of dust are required within the ionised region to absorb a fraction of the Lyman continuum. There is no difference in the physical parameters derived from present observations between *High* and *Low* detected sources. Electron density, emis-

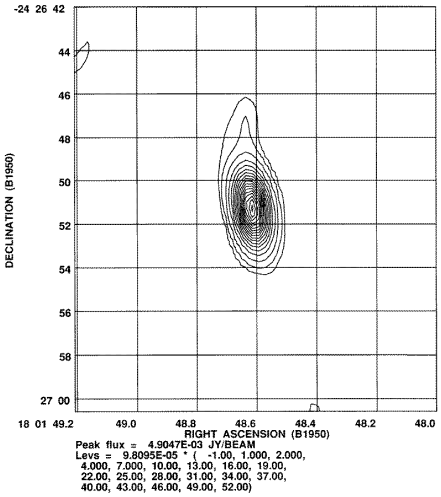

MOL37 - C

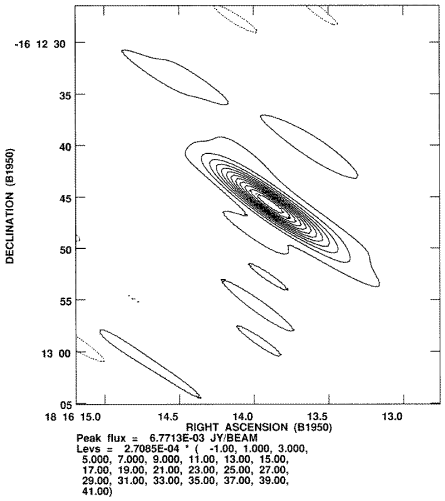

MOL50 - U

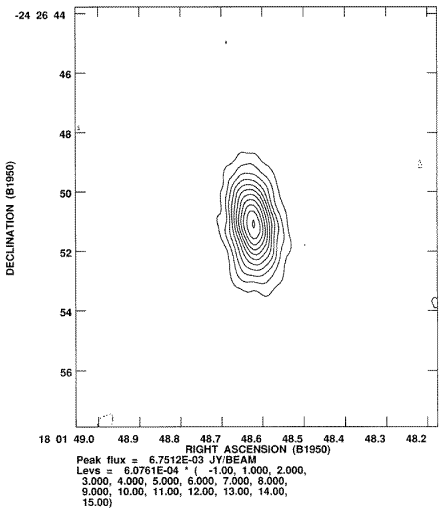

MOL37 - U

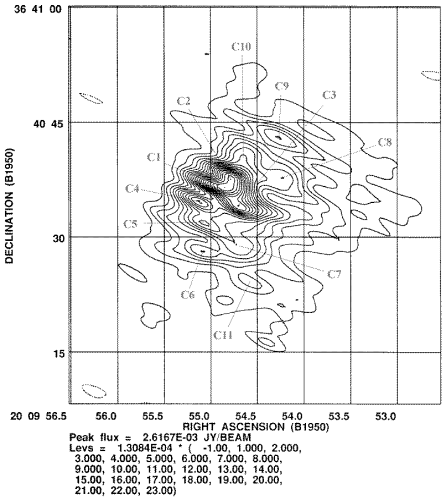

MOL117 - C

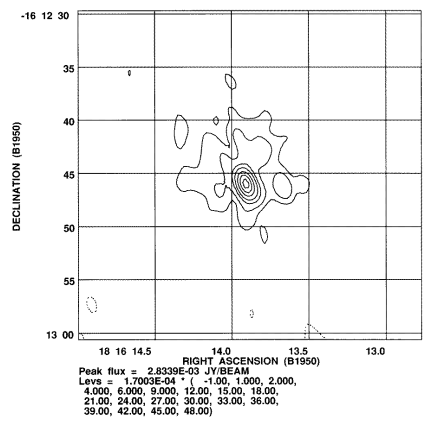

MOL50 - C

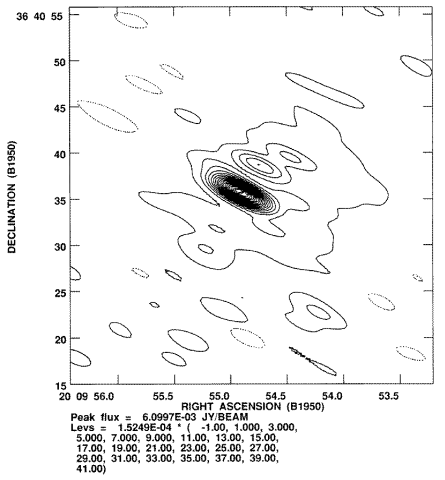

MOL117 - U

Fig. A1. Radio maps

Fig. A1. (continued)

sion measure and Lyman continuum are comparable in all the sources. From the morphological point of view, the detected radio peaks associated with IRAS sources are divided into compact or unresolved (∼55%), core-halo (∼20%) and irregular or multiply-peaked (∼25%) UC HII regions (percentages become 75%, 10% and 15% if all detected radio sources are considered); both *High* and *Low* sources are distributed in the three groups. The predominance of the sources of the first group agrees with previous results obtained by WC89, which are at the basis of the problem of the lifetime of UC HII regions.

Possibly in an earlier evolutionary stage, many sources are undetected in the radio: 76% of *Low* and 57% of *High* sources. A plausible scenario is one in which the expansion of the ionised region is effectively retarded by circumstellar matter accreting at moderate rates (less than $\sim 10^{-4}\ M_\odot\ \mathrm{yr}^{-1}$) and/or by the dust within the HII region. In spite of the fact that the number of such sources is higher (76%) in *Low* sources, also 57% of *High* sources are not revealed in radio. This "non-detection" rate for *High* sources, although higher than that observed in other radio surveys (e.g. 20% in a sample of *High*-like sources in KCW94) is compatible with the relatively lower luminosity of our sources. We also confirm that reliable medium- and high-mass protostellar candidates are preferably found in the *Low* group; in this respect the sub-sample of *Low* sources without radio counterpart is to be considered the most promising one for further studies. Submillimeter and millimeter continuum observations of these sources will be presented in a forthcoming paper, while observations with the Long Wavelength Spectrometer (LWS) onboard the Infrared Space Observatory (ISO) are being carried out at the time of writing.

Acknowledgements. We thank an anonymous referee whose comments and suggestions have improved the quality of the paper. This project was partly supported by CNR grant 97.00018.CTO2 and by ASI grant ARS96-66 to the Osservatorio di Arcetri.

Appendix A: radio maps

The complete set of maps of all detected radio peaks is presented in electronic form only. Here we give an example of each of the morphological types found (Fig. A1): Mol37 (S), Mol50 (CH), and Mol117 (I); source running number and radio band (C for λ= 6cm and U for λ= 2cm) are reported for each map.

References

Akeson R.L., Carlstrom J.E. 1996, ApJ 470, 528
Beech M., Mitalas R. 1994, ApJS 95, 517
Cesaroni R., Churchwell E., Hofner P., Walmsley C.M., Kurtz S. 1994, A&A 288, 903
Churchwell E. 1991 in *The Physics of Star Formation and Early Stellar Evolution*, eds. C.J. Lada & N.D. Kylafis (Dordrecht: Reidel Publ. Co.), p.221
Codella C., Felli M. 1995, A&A 302, 521
Codella C., Testi L., Cesaroni R. 1997, A&A , in press
DePree C.G., Rodriguez L.F., Goss W.M. 1995, Rev. Mex. de Astron. y Astrofis., 31, 39
Draine B.T., Lee H.M. 1984, ApJ 285, 89
Harju J., Walmsley C.M., Wouterloot J.G.A. 1993, A&AS 98, 51
Hofner P., Churchwell E. 1996, ApJS 120, 283
Hollenbach D., Johnstone D., Lizano S., Shu F.H. 1994, ApJ 428, 654
Hughes V.A., MacLeod G.C. 1994, ApJ 427, 857 (HML94)
Kurtz S., Churchwell E., Wood D.O.S. 1994, ApJS 91, 659 (KCW94)
McCutcheon, W.H., Dewdney, P.E., Purton, C.R., Sato, T. 1991, AJ 101, 1435
Mezger P.G., Henderson A.P. 1967, ApJ 147, 471
Miralles M.P., Rodriguez L.F., Scalise E. 1994, ApJS 92, 173
Molinari S., Brand J., Cesaroni R., Palla F. 1996, A&A 308, 573 (Paper I)
Palla F., Stahler S.W. 1990, ApJ 360, L47
Palla F., Brand J., Cesaroni R., Comoretto G., Felli M. 1991, A&A 246, 249 (P91)
Panagia N. 1973, AJ 78, 929
Panagia N., Walmsley C.M. 1978, A&A 70, 411
Richards P.J., Little L.T., Moriseva M., Heaton B.D. 1987, MNRAS 228, 43
Rodriguez L.F., Myers P.C., Cruz-Gonzalez I., Terebey S. 1989, ApJ 347, 461
Schmidt-Kaler Th. 1981, in Landolt-Börnstein, Gruppe VI, Band 2, p. 1 (Springer-Verlag)
Terebey S., Shu F.H., Cassen P. 1984, ApJ 286, 529
Testi L., Palla F., Prusti T., Natta A., Maltagliati S. 1997, A&A 320, 159
Thompson R.I. 1984, ApJ 283, 165
Walmsley C.M. 1995, Rev. Mex. de Astron. y Astrofis. Serie de Conferencias, 1, 137
Wood D.O.S., Churchwell E. 1989, ApJS 69, 831 (WC89)
Yorke H.W., Bodenheimer P., Laughlin G. 1995, ApJ 443, 199